SENSITIVITY OF BLIND PULSAR SEARCHES WITH THE *FERMI* LARGE AREA TELESCOPE

M. DORMODY[1], R. P. JOHNSON[1], W. B. ATWOOD[1], A. BELFIORE[1,2,3], I. A. GRENIER[4,7], T. J. JOHNSON[5,8],
M. RAZZANO[1,6], AND P. M. SAZ PARKINSON[1]

[1] Santa Cruz Institute for Particle Physics, Department of Physics and Department of Astronomy and Astrophysics,
University of California at Santa Cruz, Santa Cruz, CA 95064, USA; dormody@scipp.ucsc.edu
[2] Dipartimento di Fisica Nucleare e Teorica, Università degli Studi di Pavia, I-27100 Pavia, Italy
[3] INAF-Istituto di Astrofisica Spaziale e Fisica Cosmica, I-20133 Milano, Italy
[4] Laboratoire AIM, CEA-IRFU/CNRS/Université Paris Diderot, Service d'Astrophysique, CEA Saclay, F-91191 Gif sur Yvette, France
[5] National Academy of Sciences, Washington, DC 20001, USA
[6] Istituto Nazionale di Fisica Nucleare, Sezione di Pisa, and Dipartimento di Fisica "Enrico Fermi", Università di Pisa, I-56127 Pisa, Italy
[7] Institut Universitaire de France, F-75005 Paris, France

ABSTRACT

We quantitatively establish the sensitivity to the detection of young to middle-aged, isolated, gamma-ray pulsars through blind searches of *Fermi* Large Area Telescope (LAT) data using a Monte Carlo simulation. We detail a sensitivity study of the time-differencing blind search code used to discover gamma-ray pulsars in the first year of observations. We simulate 10,000 pulsars across a broad parameter space and distribute them across the sky. We replicate the analysis in the *Fermi* LAT First Source Catalog to localize the sources, and the blind search analysis to find the pulsars. We analyze the results and discuss the effect of positional error and spin frequency on gamma-ray pulsar detections. Finally, we construct a formula to determine the sensitivity of the blind search and present a sensitivity map assuming a standard set of pulsar parameters. The results of this study can be applied to population studies and are useful in characterizing unidentified LAT sources.

Key words: gamma rays: stars – pulsars: general

Online-only material: color figures

1. INTRODUCTION

The Large Area Telescope (LAT) on board the *Fermi Gamma-ray Space Telescope*[9] has currently detected close to 100 pulsars, with over 1/3 detected in blind searches of LAT data. These LAT pulsar observations are biased to nearby, bright pulsars, with photon fluxes above 100 MeV (F_{100}) typically above 10^{-8} photon cm^{-2} s^{-1}. Such gamma-ray pulsars tend to have double-peaked pulse profiles and spectra with exponential energy cutoffs. They are also young to middle-aged ($\tau_C < 10$ Myr), energetic ($\dot{E} > 10^{33}$ erg s^{-1}), and have large surface magnetic fields ($B_S > 10^{11}$ G).

To be detectable in blind searches, such pulsars must have a large number of pulsed photons and a relatively small number of background photons (e.g., diffuse gamma rays, neighboring sources). In addition, the accuracy of the initial search position, relative to the true pulsar position, also plays a key role in the detectability of a pulsar. The precise detectability threshold as a function of these various parameters is something that has not yet been properly quantified. Establishing the sensitivity to pulsation detections allows for population studies of gamma-ray pulsars (M. Dormody et al. 2011b, in preparation), as well as setting upper limits on pulsations from unidentified *Fermi* LAT sources.

Most pulsar searches in radio, X-ray, optical, and gamma rays involve looking for periodic signals in the frequency domain by performing Fourier transformations of time series (e.g., Lorimer & Kramer 2004). The main difficulty in detecting pulsars in gamma rays alone is that gamma-ray observations have very few photons when compared with radio or X-ray observations, requiring long integration times in order to collect enough signal. The number of bins, N, in the discrete Fourier transform (DFT) grows linearly with time as $N = 2 f_{\max} T$, where $f_{\max}$ is the maximum search frequency and T is the length of the viewing period. In addition, pulsars gradually spin down with a non-negligible frequency derivative $\dot{f}$ as they radiate energy, requiring the computation of tens of thousands of DFTs to scan a typical f–$\dot{f}$ space, which is computationally intensive. We instead search for a signal in the *time differences* out to a maximum time window T_{maxdiff}. This method effectively resets the clock on the photon times which reduces the effect of phase walk, and also reduces the number of DFT bins and $\dot{f}$ trials. The slight reduction in Fourier power caused by this non-coherent technique compared with a fully coherent DFT is compensated for by having fewer frequency bins N and fewer $\dot{f}$ trials (Atwood et al. 2006).

We establish the detection probability using a large-scale simulation of a search for gamma-ray pulsars across a broader parameter space than that observed, including the estimation of source position using the same detection and localization tools in the *Fermi* LAT Bright Gamma-ray Source List (0FGL; Abdo et al. 2009b) and the *Fermi* LAT First Source Catalog (1FGL; Abdo et al. 2010a). The blind search resulted in the discovery of 26 previously unknown pulsars (Abdo et al. 2009a; Saz Parkinson et al. 2010; P. M. Saz Parkinson et al., in preparation). This analysis discusses the sensitivity of this specific blind search technique and does not apply to other blind search techniques (Pletsch et al. 2011). While the pulsar flux sensitivity for radio detections has been established using the modified radiometer equation for a given telescope (Lorimer & Kramer 2004), the analogous sensitivity threshold for gamma-ray pulsars discovered using only gamma rays has not yet been established. This threshold is distinct from the sensitivity of gamma-ray pulsar searches using known timing solutions from other wavelengths (e.g., radio or X-ray), for which the

---

[8] National Research Council Research Associate. Resident at Naval Research Laboratory, Washington, DC 20375, USA.
[9] http://fermi.gsfc.nasa.gov/

sensitivity is expected to be improved due to the fewer search trials (Razzano & Harding 2007).

We developed a method to establish the sensitivity of the blind search technique of detecting gamma-ray pulsars using a Monte Carlo simulation to characterize unidentified LAT sources and aid in pulsar population studies. This paper is organized as follows. In Section 2, we detail the source simulation, including the positions, spectral, and rotational parameters for each simulated pulsar. In Section 3, we discuss the technique to localize *Fermi* LAT sources and the specific details of the blind search. In Section 4, we present the results of the blind searches, including the effect of positional error and the definition of a detectability metric M. We also discuss the benefits of using counterpart source locations to improve the sensitivity. In Section 5, we interpret the results by modeling the sensitivity using the metric M and determine an all-sky sensitivity map. We conclude in Section 6 and discuss future improvements to our blind searches.

2. CREATING THE SIMULATED PULSAR POPULATION

Each simulated pulsar is fully described by its rotational and spectral parameters, as well as its location on the sky. The rotational parameters include the rotational spin frequency f, frequency derivative $\dot{f}$, epoch of the ephemeris, and pulse profile. Gamma-ray pulsar spectra are well modeled by a power law with an exponential cutoff (Abdo et al. 2010c). Each pulsar location is specified by Galactic coordinates (l, b). The pulsars are not simulated with timing irregularities or higher order frequency derivative terms.

In contrast with existing Galactic pulsar population models (e.g., Gonthier et al. 2004; Harding et al. 2007), we adopt a pulsar model that samples the known gamma-ray pulsar pulse profile distribution without regard to emission mechanism or evolution. The pulsars in this study are simulated only to measure the blind search sensitivity and we have therefore not restricted ourselves to a parameter space that might be considered realistic from a point of view of pulsar physics. For instance, several older pulsars ($\tau > 10$ Myr) are simulated with very large frequency spin-downs ($\dot{f}$). If $\dot{f} = -10^{-11}$ Hz s^{-1}, then $\dot{E} \sim 5 \times 10^{39}$ erg s^{-1}, which is far above the largest known pulsar spin-down $\dot{E}$ (the Crab pulsar has $\dot{E} = 4 \times 10^{38}$ erg s^{-1}). While these sources are unphysical, pulsars with these parameters can help to quantify the observational bias seen in the observed spin parameter space.

Pulsars are created using the programs *PulsarSpectrum* (Razzano et al. 2009) and *gtobssim*.[10] *PulsarSpectrum* simulates LAT gamma-ray pulsar photons from a given pulsar spectrum and rotational ephemeris. It uses the instrument response functions (IRFs) of the LAT to generate realistic photon arrival times. For this study we use the P6_V3 *diffuse* IRFs and simulate one year of *diffuse* class photons (Atwood et al. 2009) from 2008 August 4 through 2009 August 4 (MJD 54682−55047). *Diffuse* class photons are optimal for non-variable, steady sources because they have the best point-spread function (PSF) and lowest level of charged particle contamination.

The background used in the simulation is the actual data collected by the LAT in the same time range, processed with the same Pass 6 event selections. This is the first year of LAT sky-survey mode and corresponds to the data set used to find the first 26 blind search pulsars. The use of real LAT data as our background avoids possible biases from incorrect modeling of the

Galactic and extragalactic diffuse components. 1FGL sources located within the region of interest (ROI) of the simulated pulsar can lead to source confusion, especially for fainter simulated pulsars. The inability to disentangle simulated pulsar photons from 1FGL sources as well as Galactic and extragalactic diffuse emission directly affects the source detectability, which is discussed in more detail in Section 3.1.

2.1. Timing Model

Observed pulsars emitting radio and/or gamma rays do not uniformly cover the f–$\dot{f}$ space. The LAT has so far only observed pulsations from pulsars with $f > 2$ Hz and $|\dot{f}| < 3.7 \times 10^{-10}$ Hz s^{-1}. We uniformly sample a broader region of the f–$\dot{f}$ parameter space to quantify the observational bias. Our simulated pulsars sample the spin parameter space in a log-uniform random distribution with $(0.1 \leqslant f \leqslant 64)$ Hz, and $(10^{-15} \leqslant -\dot{f} \leqslant 10^{-10})$ Hz s^{-1} (see shaded region in Figure 1). In this fashion, the Crab is the only LAT pulsar not covered in the simulation. We are not sampling the *recycled* pulsar domain (i.e., millisecond pulsars, MSPs) and keep to the normal population of younger pulsars. Within the sampled range, if pulsars are systematically detected in a region of the parameter space where they are not observed by the LAT, these objects do not occur in nature. Conversely, if pulsars are systematically not detected in a region of the parameter space, we cannot infer any conclusion about the underlying pulsar population. Observed ratio pulsars in the ATNF (Australia Telescope National Facility) database[11] (Manchester et al. 2005) cover a part of the simulated parameter space not observed in gamma rays, especially at lower $\dot{E}$.

We select the epoch to be in the middle of the year-long observation (MJD 54866). This choice minimizes the covariances between timing model parameters. Young and middle-aged pulsars can exhibit *glitches* (Espinoza et al. 2011; M. Dormody et al. 2011a, in preparation), an abrupt increase in spin frequency. They can also exhibit *timing noise* (Edwards et al. 2006; Ray et al. 2011), smooth deviations from the expected linear spin-down. Any or all of these effects can hamper detections, but we do not include them in our simulations as including these effects is beyond the scope of this study.

2.2. Pulse Profile

We select the pulse profile based on the general features in the pulse profiles of the known gamma-ray pulsars: broad, mostly double-peaked (Abdo et al. 2010c). We assume no spectral modulation in phase and fix the pulse profile to be the same across all energies, which is modeled by the sum of two Lorentzians and a constant:

$$n(\phi) = \frac{I_1}{1 + ((\phi - \phi_1)/w_1)^2} + \frac{I_2}{1 + ((\phi - \phi_2)/w_2)^2} + n_0. \quad (1)$$

Here, the phase ϕ ranges from $0 \leqslant \phi \leqslant 1$. I_1 and I_2 are the amplitudes of the two peaks and are selected from a random, uniform distribution between 0 and 100. This can lead to a single-peaked profile if one amplitude happens to be sampled low enough. The unpulsed component n_0 is selected from a random, uniform distribution between 0 and 25. The widths of the peaks are fixed at $w_1 = 0.01$ and $w_2 = 0.015$. The phase separations of the peaks are fixed at $\phi_1 = 0.25$ and $\phi_2 = 0.65$. The parameters used in the pulse profile template in Equation (1) are reasonable based on LAT observations of gamma-ray pulsars

---

[10] http://fermi.gsfc.nasa.gov/ssc/

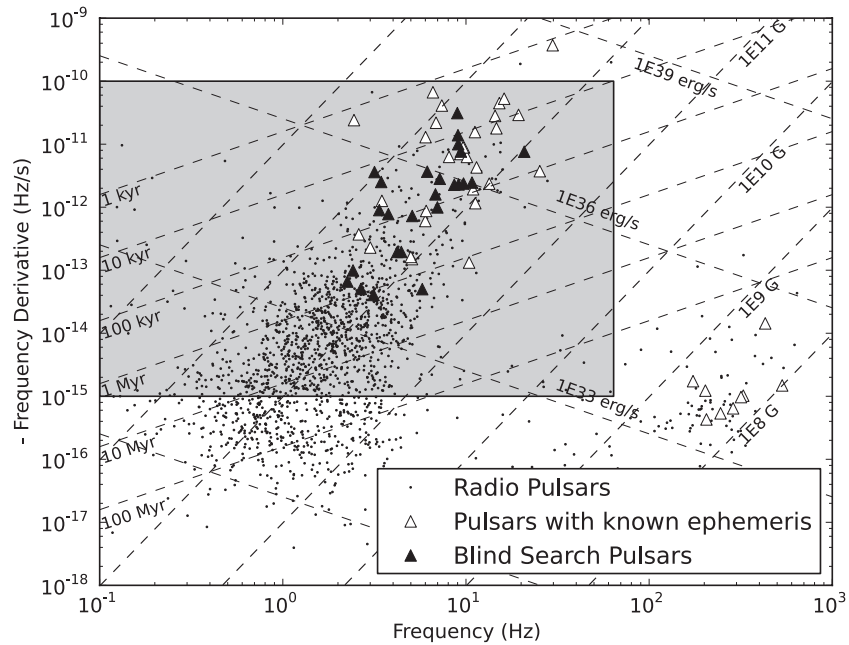[11] http://www.atnf.csiro.au/people/pulsar/psrcat/

Figure 1. Spin parameter space for ~1800 pulsars in the ATNF pulsar catalog (Manchester et al. 2005) and 54 *Fermi* LAT gamma-ray pulsars included in the First Fermi Pulsar Catalog and Blind Search discovery papers (Abdo et al. 2010c; Saz Parkinson et al. 2010). Black triangles indicate blind search gamma-ray pulsars (including Geminga), and white triangles indicate gamma-ray pulsars with a known ephemeris. Black dots indicate all known radio pulsars. The three sets of dashed lines indicate characteristic age, surface magnetic field strength, and rotational spin-down energy. The shaded region indicates the spin parameter space all simulated pulsars are drawn from.
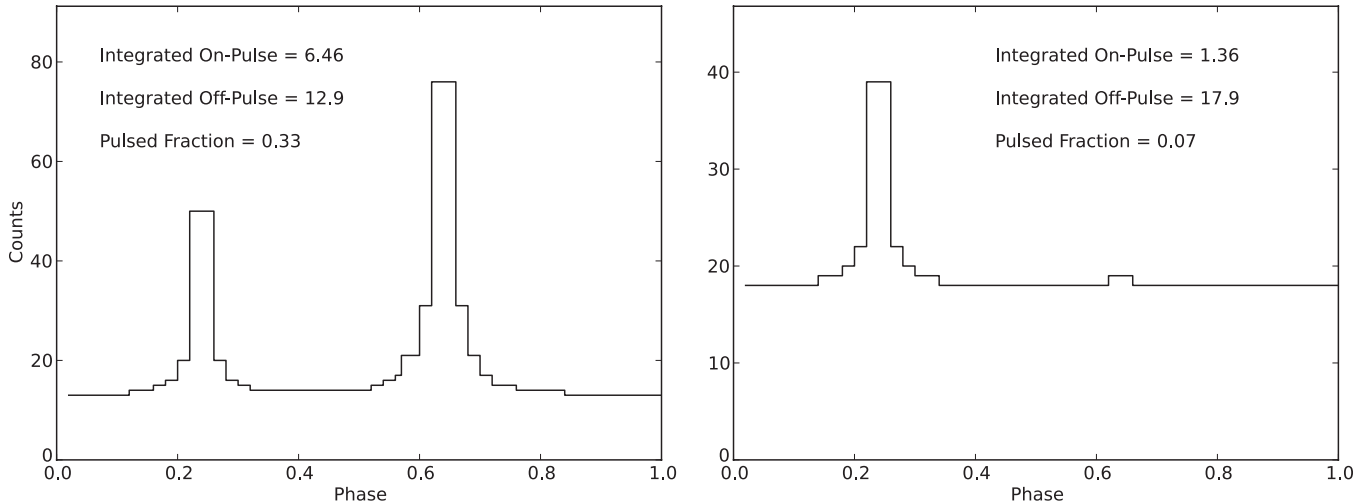

Figure 2. Pulse profiles for two simulated pulsars. Note how the left profile has a small unpulsed component whereas the right profile has a large unpulsed component, contributing to different values of the pulsed fraction.

(Abdo et al. 2010c). While the separation of the peaks can affect the detectability of a pulsar, the majority of observed gamma-ray pulsars have peak separations $\Delta \sim 0.4$–0.5. The pulse profile is sampled to 50 bins in phase across one rotation.

The pulsed fraction PF is calculated by integrating the pulsed portion of Equation (1) and dividing by the integral of the pulsed and unpulsed portion:

$$\mathrm{PF} = \left[1 + \frac{n_0}{\pi (I_1 w_1 + I_2 w_2)} \right]^{-1}, \qquad (2)$$

where $0 \leqslant \mathrm{PF} \leqslant 1$. In Figure 2, we show two examples of pulse profiles: one has a large PF and the other has a small PF. While the pulse profiles sampled here cover a wide range of gamma-ray profiles, they do not cover profiles with three or more peaks,

narrowly separated peaks, or very broad peaks that are difficult to disentangle from the unpulsed component. In addition, some LAT pulsars exhibit an energy-dependent pulse profile, but this is not incorporated into this simulation since these represent a small number of exceptional cases.

2.3. Spectral Model

Gamma-ray pulsar spectra are well modeled by a power law with an exponential cutoff (Abdo et al. 2010c):

$$\frac{dN}{dE\,dA\,dt} = C \left(\frac{E}{1\,\mathrm{GeV}} \right)^{-\Gamma} \exp\left[-\left(\frac{E}{E_{\mathrm{cutoff}}} \right)^{\beta} \right], \qquad (3)$$

where the spectral parameters include the spectral index Γ, cutoff energy E_{cutoff}, cutoff index β ($\beta < 1$ for sub-exponential,
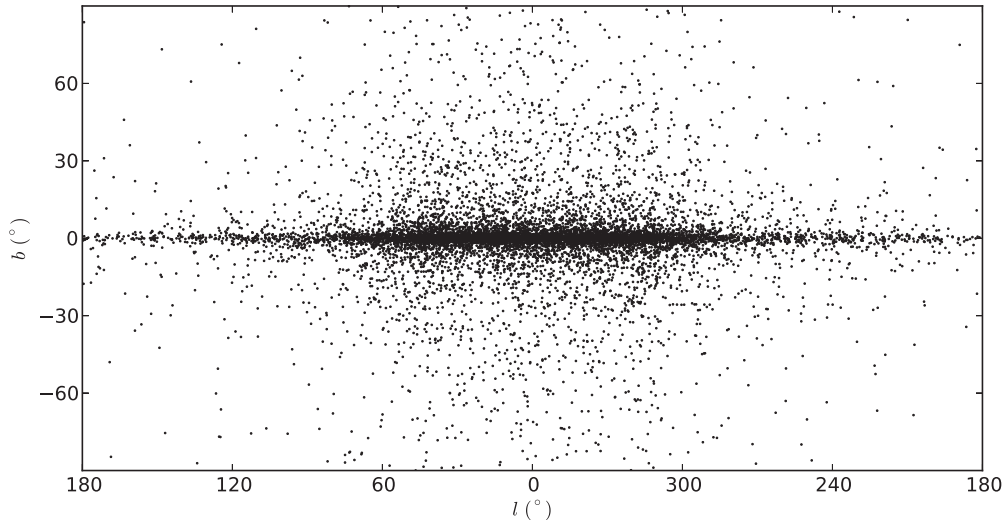
Figure 3. Source locations of all 10,000 pulsars simulated according to the distribution described in Section 2.4. Each pulsar was simulated and then searched one at a time to avoid source confusion.

$\beta > 1$ for super-exponential), and normalization factor C. While the brightest pulsars are known to have phase-dependent energy spectra (Abdo et al. 2009c, 2010d), we assume a uniform, phase-averaged spectrum. Since pulsar detections are carried out over a wide energy band, such spectral variations are second-order effects. In addition, *Fermi* LAT pulsars can be associated with supernova remnant and pulsar wind nebula sources, which can affect the measured unpulsed spectrum and flux stability of the pulsar source (Ackermann et al. 2011; Abdo et al. 2011).

We vary Γ, E_{cutoff}, and β uniformly over the ranges ($0.6 \leqslant \Gamma \leqslant 2.1$), ($1 \leqslant E_{\text{cutoff}} \leqslant 2$) GeV, and ($0.5 \leqslant \beta \leqslant 4.5$), respectively. Gamma-ray pulsars have spectral indices spanning this range, and cutoff energies between (0.7 ± 0.5) GeV (PSR J0659+1414) and (5.8 ± 0.5) GeV (Crab pulsar), which is much wider than the sampled cutoffs. Since the pulsar spectral parameters are only used to determine the number of pulsar photons, and all photons are weighted equally in the blind search, the narrow sampling of E_{cutoff} is sufficient for pulsar spectra in this simulation. In addition, Equation (3) can model the exponential cutoff ($\beta = 1$) predicted by magnetospheric emission models or the super-exponential cutoff ($\beta > 1$) predicted by the polar cap emission model and the low-altitude slot gap model (Muslimov & Harding 2003). We sample below $\beta = 1$ as some *Fermi* LAT pulsars exhibit a sub-exponential cutoff (Abdo et al. 2010b).

Pulsars are detected in blind searches from $F_{100} \sim 10^{-5}$ photon cm^{-2} s^{-1} (Vela) down to $F_{100} = 6 \times 10^{-8}$ photon cm^{-2} s^{-1} (J2032+4127; Abdo et al. 2010c), where F_{100} is the flux of the source above 100 MeV. We sample our simulated pulsars in a log-uniform, random distribution of ($10^{-9} \leqslant F_{100} \leqslant 10^{-6}$) photon cm^{-2} s^{-1}. This allows us to explore the detectability of high-flux pulsars with different spectral models, as well as establish the sensitivity threshold. We obtain the normalization factor C by integrating the spectrum in Equation (3) over all energy bins:

$$F_{100} = C \int_{0.1\,\text{GeV}}^{20\,\text{GeV}} \left(\frac{E}{1\,\text{GeV}}\right)^{-\Gamma} \exp\left[-\left(\frac{E}{E_{\text{cutoff}}}\right)^{\beta}\right] dE.$$

(4)

We only integrate up to 20 GeV as few photons contribute to the flux above this energy range.

2.4. Source Locations

Most pulsars lie within the Galactic plane ($|b| < 5°$). This is usually explained by the fact that young and middle-aged pulsars have not had time to move far from their birth locations in the plane (Paczynski 1990). We sample our simulated pulsar source locations from the (l, b) distribution of the known pulsar population in the ATNF database. The probability distribution is modeled with a broken power law for l and $|b|$:

$$p(x) = \begin{cases} x^{\alpha_1}/\alpha_1 & x < B \\ B^{\alpha_1}/\alpha_1 + B^{\alpha_1-\alpha_2}/\alpha_2 \times (x^{\alpha_2} - B^{\alpha_2}) & \text{otherwise.} \end{cases}$$

(5)

For $180° \leqslant l \leqslant 360°$, $x = 360 - l$, $\alpha_1 = 0.9998$, $\alpha_2 = -1.45$, $B = 44.87$, and for $0° \leqslant b \leqslant 90°$, $x = |b|$, $\alpha_1 = 0.75$, $\alpha_2 = -0.26$, $B = 1.23$. These values were obtained with a fit to the pulsars in the ATNF database. While this selection includes MSPs ($f > 100$ Hz) which tend to have a broader latitude distribution, they comprise only $\sim$10% of pulsars and only affect the fit parameters by a few percent. We assumed symmetry around the Galactic meridian $l = 0$ and $b = 0$ (see the plot of the simulated positions in Figure 3).

3. SOURCE ANALYSIS AND BLIND SEARCH

We establish a procedure to replicate the one adopted to generate both the 0FGL (Abdo et al. 2009b) and 1FGL (Abdo et al. 2010a) catalogs and to discover the 26 blind search pulsars. In order to realistically measure the blind search sensitivity, we must use source locations derived exclusively from *Fermi* LAT photons. Here we describe the localization tools and methods used in the construction of the 0FGL and 1FGL catalogs. We also describe the event selection and search parameters in the blind search, and the criteria for detection.

3.1. Source Detection and Localization Methods

Since the blind search relies on source positions, i.e., it is not *positionally* blind, pulsations are easier to detect from bright, well-localized pulsars. Conversely, pulsations are more difficult to detect from faint, poorly localized pulsars. We localize the simulated pulsars according to the procedure described in Abdo et al. (2009b, 2010a). We bin the photon data into three

overlapping energy bands: *Front*[12] events with $E > 200$ MeV or *Back* events with $E > 400$ MeV and $0\overset{\circ}{.}3$ pixels; *Front* events with $E > 1$ GeV or *Back* events with $E > 2$ GeV and $0\overset{\circ}{.}2$ pixels; and *Front* events with $E > 5$ GeV or *Back* events with $E > 10$ GeV and $0\overset{\circ}{.}1$ pixels. We used two different wavelet detection methods: *mr_filter* (Starck & Pierre 1998) and *PGWAVE* (Damiani et al. 1997; Ciprini et al. 2007). For *mr_filter*, the False Discovery Rate (Benjamini & Hochberg 1995) was set to 1.2% (2.5σ) in the first two bands and 0.27% (3σ) in the highest energy band. We used SExtractor (Bertin & Arnouts 1996; Holwerda 2005) to extract the sources from the *mr_filter* output. *PGWAVE* returns a list of source seeds directly.

We also used *pointfind*, a tool that searches for candidate point sources by maximizing a likelihood function for trial point sources at each direction in a HEALPix (Górski et al. 2005) order 9 tessellation of the sky ($0\overset{\circ}{.}1 \times 0\overset{\circ}{.}1$ pixels). The *pointfind* algorithm divides the data into four energy bins per decade and determines the significance of a trial point source against the diffuse background in each pixel. Further trials optimize the likelihood with respect to the signal fraction. A second pass uses a more complicated likelihood function incorporating nearby point sources. For each source, *pointfind* generates a Test Statistic (TS) map. The TS is defined as $2(\log L_{\max} - \log L(p))$, where p is the source position and $L_{\max}$ is the maximum value of the likelihood $L(p)$. Contours of source location probability are defined by interpreting deviations of T from a peak value (i.e., the maximum likelihood position of a pulsar) in terms of a χ^2 distribution with 2 degrees of freedom, and can be used to reject positions falling below a given confidence threshold. We extract the positions of candidate point sources (seeds) from the TS maps (Abdo et al. 2010a).

We considered two localization tools to refine the coarse seed positions: *pointfit* and *gtfindsrc*.[13] The tool *gtfindsrc* is not optimal for this study, as it can only perform an unbinned likelihood analysis, which is prohibitive for one year of photon data and thousands of sources. It also requires a large overhead in the form of individual exposure maps and maps of the diffuse model convolved with the IRF. We used a Galactic diffuse model designated *54_86Xexph7S* calculated using GALPROP,[14] an evolution of that used in the 0FGL. A similar model, *gll_iem_v02*, is publicly available.[15] The *pointfit* tool performs the same task but only requires a diffuse background model and a photon data file. Thus, we used *pointfit* for this step in the analysis. We compared these two methods using a sample of 100 simulated pulsars and found that the localizations were consistent with each other.

The *pointfit* tool is similar to *pointfind* in that it is a likelihood analysis tool that maximizes a binned likelihood function and returns source locations along with TS values. However, it is used for source localizations of seed detections, obtained from *mr_filter*, *PGWAVE*, and *pointfind*. The overall likelihood function L is the product of the energy band likelihoods L_i. The choice of *pointfind* and *pointfit* is used in order to align closely with the procedure in the 1FGL catalog.

The detection of our simulated sources, as in the case of real sources, depends on the source flux and position. As shown in Figure 4, bright sources tend to be well localized (upper left plot). Moderately bright sources located within the diffuse emission along the Galactic plane or near other bright pulsars can be affected by source confusion, which can worsen the localization (upper right plot). Faint pulsar sources, while formally detected just above the threshold (TS = 25) are poorly localized (lower left plot), and extremely faint pulsars are not detected at all (lower right plot). It is safe to assume a source not reasonably localized would not be detected as a pulsar in a blind search. In order to restrict our searches to reasonably localized sources, we perform the blind search only on sources localized to within $2°$ of the simulated location. This is a fairly conservative criterion, as all sources included in the 1FGL catalog have a 95% error radius smaller than $0\overset{\circ}{.}6$ (Abdo et al. 2010a).

While source localizations from gamma-ray observations are limited by the relatively broad PSF and limited photon statistics, observations from other wavelengths can have much finer spatial resolution and allow for precise source localization. For gamma-ray pulsars with possible counterpart locations (e.g., X-ray or radio observations) we can perform searches for pulsation at these more precise positions to aid in blind searches. We investigate the effect of precise source locations on blind search detectability in Section 5.1.

3.2. The Blind Search

We replicate the analysis from Abdo et al. (2009a), Saz Parkinson et al. (2010), and P. M. Saz Parkinson et al. (in preparation) using the same code, settings, and search strategy. The specific blind search method in this analysis searches the time differences of photons from simulated pulsars using a maximum time-differencing window of $T_{\mathrm{maxdiff}} = 2^{19}$ s ($\sim$6 days). We perform a fast Fourier transform (FFT) between 0.1 and 64 Hz with photon times corrected for the spin-down $\dot{f}$:

$$t' = t + \frac{1}{2}\frac{\dot{f}}{f}t^2, \tag{6}$$

where $\dot{f}$ is rounded to the search resolution of $\Delta\dot{f} = 1/(2T_v T_{\mathrm{maxdiff}}) \approx 3 \times 10^{-14}$ for one year of observations, and T_v is the one year viewing period. We used an ROI in the photon selection ($r \leqslant 0\overset{\circ}{.}8$, $E_{\min} = 300$ MeV, P6_V3 *diffuse* class photons, with zenith angle $\leqslant 105°$ to avoid photons from Earth's limb). We corrected the photon event times from each source to the solar system barycenter using *gtbary*, assuming all photons come from the source positions given by the LAT localization tools as described in Section 3.1. We look for promising candidates for follow-up based on of the following two criteria.

1. The Fourier power has a probability of false detection of $p < 10^{-4}$, taking into account the number of bin trials in the FFT of the time differences.
2. After a fully coherent refinement, the pulse profile with 32 bins has $\chi^2 \geqslant 5$ for 31 degrees of freedom when compared with a flat distribution.

We confirm the detection by checking the value of the detected frequency with the simulated frequency: $f_{\mathrm{simulated}} - f_{\mathrm{detected}} < 10^{-5}$ Hz, or $2T_{\mathrm{maxdiff}} \times 10^{-5} \approx 10$ frequency bins. This is a conservative estimate, as we do not expect to detect a pulsar if its frequency is shifted by more than a few bins.

After all sources are flagged as detections or non-detections, we remove duplicate detections due to multiple source locations from the seed detections, a frequent occurrence for bright

---

[12] *Front* and *Back* events indicate where in the LAT tracker the photons pair convert. *Front* events have gamma-ray conversions in the thin converter foils, which optimize the PSF at low energies, and *Back* events have gamma-ray conversions in the thicker converter foils, which maximize the effective area for photon collection. The LAT point-source sensitivity is balanced between *Front* and *Back* events (Atwood et al. 2009).
[13] http://fermi.gsfc.nasa.gov/ssc/data/analysis/scitools/overview.html
[14] http://galprop.stanford.edu/
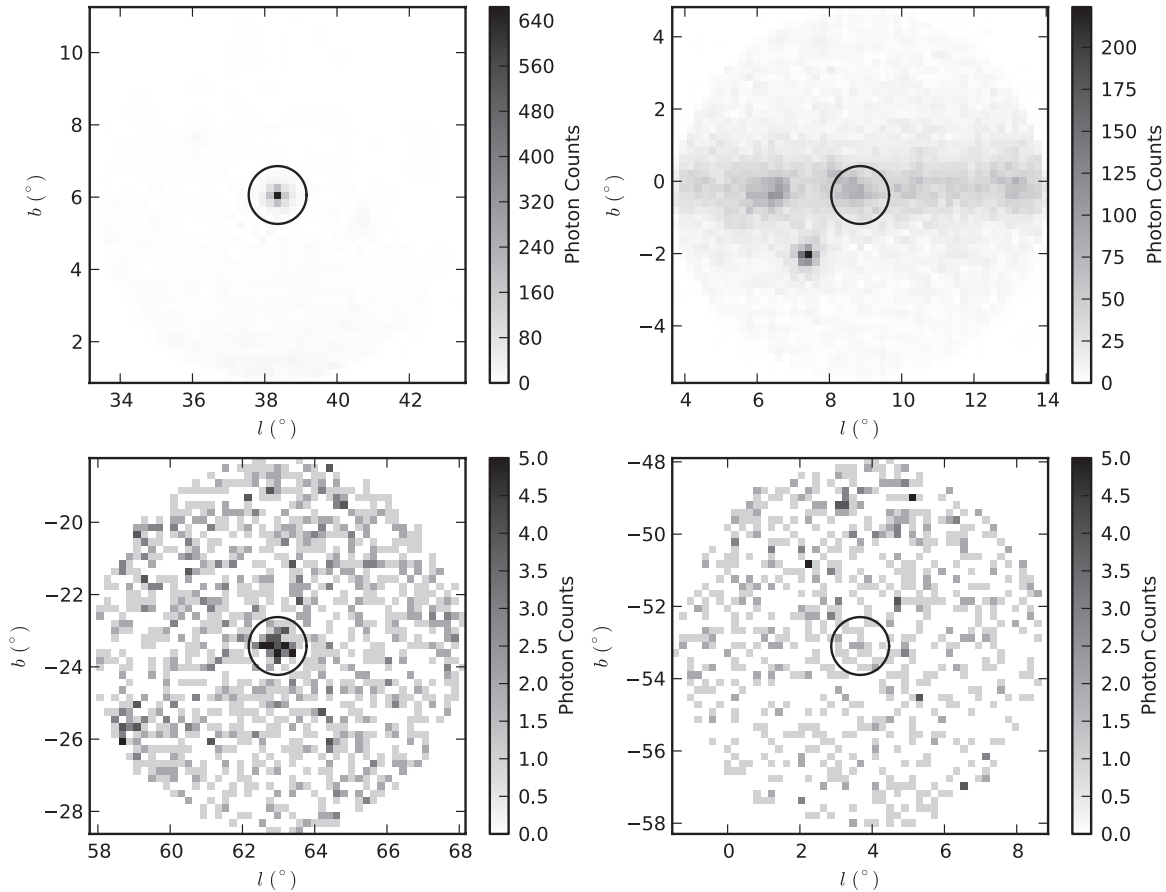[15] http://fermi.gsfc.nasa.gov/ssc/

Figure 4. Count maps for four different simulated pulsars, illustrating different source localizations. Each map features a simulated pulsar at the center of the circle. The upper left image is a source with good localization and highly significant detection. The upper right image is a source located within the Galactic plane and can have reduced source location precision owing to the bright diffuse emission and nearby bright sources. The lower left image is a faint gamma-ray source with a flux that lies just above the detection threshold (TS = 25). If this source had an X-ray or radio counterpart, it would enhance the blind search detectability. The lower right image is an extremely faint pulsar that is not detected as a gamma-ray source (TS < 25).

sources in confused backgrounds. We also remove faint candidates that are within a few degrees of bright pulsars (e.g., Vela, Geminga, and Crab) that are simulated with a similar $\dot{f}/f$ as these bright pulsars (<1% of simulated pulsars). These pulsars would require non-standard ways of extracting the pulsed emission of the faint pulsar from the bright pulsar.

4. RESULTS

We describe here the results obtained by applying the procedure described in Section 3 to the 10,000 pulsars simulated as described in Section 2. We confirm the trend observed in the 1FGL catalog that correlates the positional error with the TS. We define a detectability metric M in terms of pulsed fraction and signal-to-noise ratio (S/N) that fully determines the strength of the pulsation. We observe a drop-off in the sensitivity at high frequencies, which is more apparent for weaker pulsars.

The procedure described above detects sources at TS > 25 for 8138 sources within $r \leqslant 2°$, dropping to 4540 sources within $r \leqslant 0°.6$. Of these, only 1121 sources show pulsations in our blind searches, according to the detection criteria in Section 3.2, with the largest positional offset being 0°.62 for a detected pulsar. The plot of TS and positional offset for all sources with TS > 25 is shown in Figure 5. This plot illustrates that pulsars detected with higher TS values have smaller positional offsets.
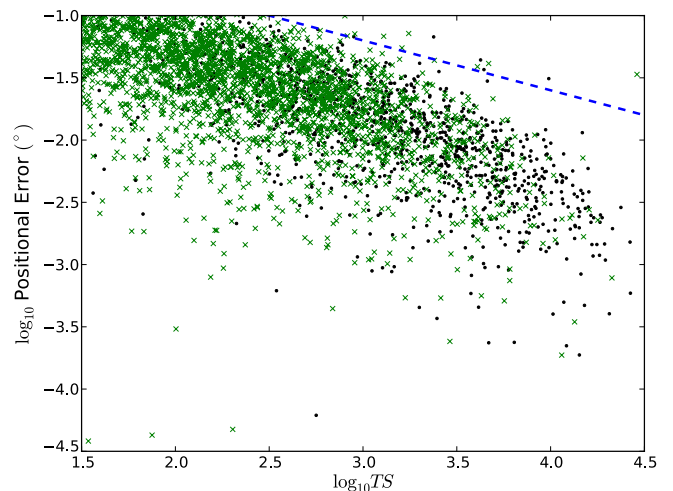

Figure 5. Positional Error vs. Test Statistic (TS) for detected pulsars (dots) and non-detections (crosses) for all sources localized to within 0°.1, with the trend $\epsilon = TS^{-0.4}$ as a dashed blue line. The dispersion for a given TS is partly due to the diffuse gamma-ray emission at the source position and the source spectrum, as hard-spectrum sources are better localized than soft sources because the PSF is narrower at high energy. Compare with Figure 2 in the 1FGL catalog (Abdo et al. 2010c).

(A color version of this figure is available in the online journal.)

The sensitivity of our blind searches to pulsar detections is almost uniform in the f and $\dot{f}$ ranges, $(0.1 \leqslant f \leqslant 16)$ Hz and
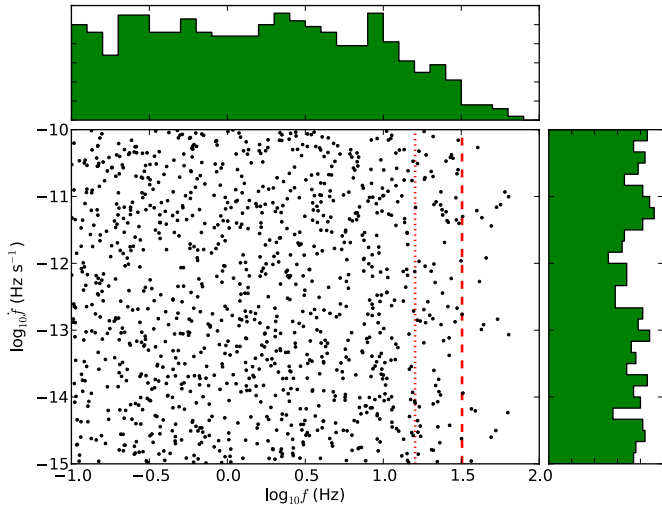
Figure 6. Spin parameters of all simulated pulsars detected in the blind search up to a maximum frequency of 64 Hz. The histogram of f at the top illustrates the detectability cutoffs above 16 Hz (dotted line) and 32 Hz (dashed line), attributed to a combination of higher sensitivity to position error at large f and fewer harmonics being combined for $f > 16$ Hz. We do not observe slow pulsars with the LAT ($f < 2$ Hz), which likely indicates that slow pulsars are not bright gamma-ray emitters. However, the lack of young, high-frequency pulsars is not due to an observational bias.

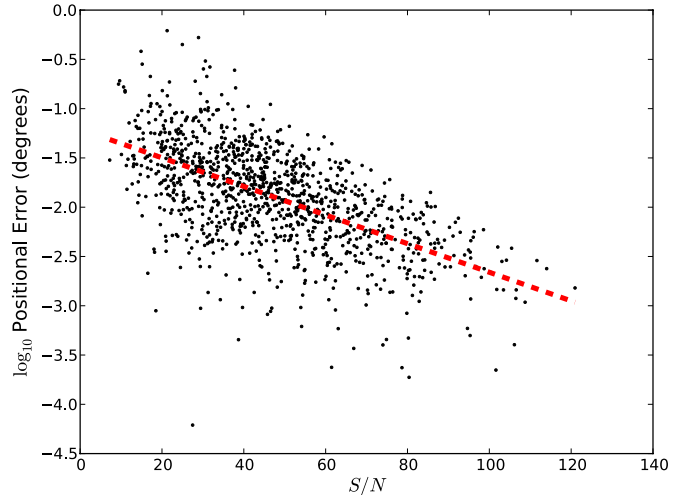(A color version of this figure is available in the online journal.)

Figure 7. Positional error (in degrees) vs. S/N for all detected pulsars. The red dashed line indicates the trend $\sigma \sim e^{-0.034 \times S/N}$, obtained from a fit to the data. The lower the S/N, the larger the position uncertainty and thus the larger the position offset. Conversely, for a source with a large S/N, the position uncertainty is smaller and the position offset is smaller.

(A color version of this figure is available in the online journal.)

$(10^{-15} \leqslant -\dot{f} \leqslant 10^{-10})$ Hz s^{-1}, respectively. The detectability of a pulsar does not depend on its spin-down $\dot{f}$, but there is a drop-off in the sensitivity of the search for $f > 16$ Hz (see Figure 6). We discuss the factors affecting detections of high-frequency pulsars in Section 5.2.

4.1. Positional Errors

The simulated pulsars reveal that the lower the S/N, the larger the uncertainty in the position, and thus the average offset, as shown in Figure 7. If we model the observed position as a two-dimensional Gaussian distribution centered at the correct position, the offset in position can be approximated by another Gaussian distribution, peaked at σ, and with a width σ. This result confirms the behavior already reported in Figure 2 in the 1FGL catalog (Abdo et al. 2010c), where the position offset has a strong dependence on the TS. Assuming an exponential dependence of σ with respect to the S/N, we fit the data to obtain a value for the exponential index:

$$\sigma \, (S/N) \sim e^{-0.034 \times S/N}. \qquad (7)$$

4.2. Detectability Metric

A pulsed signal is detected from a source if there is a large enough portion of pulsed photons. We define the detectability of the pulsar using the metric M as the logarithm of the ratio of pulsed photons to the square root of all photons:

$$M = \log_{10} \frac{n_{\mathrm{pulsed}}}{\sqrt{n}}, \qquad (8)$$

where n_{pulsed} is the number of signal photons contained in the pulse, or are above the unpulsed background in the pulse profile, and $n = n_{\mathrm{signal}} + n_{\mathrm{background}}$. We use a logarithm in the definition of M to better observe the detectability of weaker sources with lower S/Ns. Pulsed and unpulsed photons are together classified as signal photons, or $n_{\mathrm{signal}} = n_{\mathrm{pulsed}} + n_{\mathrm{unpulsed}}$. Pulsed photons

can be selected by phase cuts, and unpulsed photons can be distinguished from the background by the spectral model and PSF angular distribution. The detectability of the pulsar does not directly depend on n_{pulsed}, n_{unpulsed}, or $n_{\mathrm{background}}$, but only on the metric M. This is motivated by the indistinguishability of n_{unpulsed} and $n_{\mathrm{background}}$ as shown in Figure 8: an unpulsed background is composed of unknown portions of background diffuse photons and unpulsed pulsar photons.

If the number of pulsed photons is known from the pulse shape a priori, M is calculated easily using Equation (8). However, if the pulse profile is unknown, M is calculated by estimating the PF and using a spectral model to calculate the S/N:

$$M = \log_{10} \left(\underbrace{\frac{n_{\mathrm{pulsed}}}{n_{\mathrm{pulsed}} + n_{\mathrm{unpulsed}}}}_{\mathrm{PF}} \times \underbrace{\frac{n_{\mathrm{signal}}}{\sqrt{n_{\mathrm{signal}} + n_{\mathrm{background}}}}}_{\mathrm{S/N}} \right). \qquad (9)$$

The expected number of signal photons n_{signal} from a source falling within a given ROI can be determined from the pulsar spectrum, flux, and IRFs. We select diffuse class photons satisfying the following cuts: $r \leqslant 0°.8$, where r is the angular separation from the source position; $E \geqslant 300$ MeV, *diffuse* class photons. The 68% containment angle θ_{68} for normal incidence ($\cos\theta > 0.9$) of the *front* and *back* converters (see Section 3.1) for P6_V3 *diffuse* photons[16] can be fitted with a third-order polynomial function given by a fit to the PSF:

$$\log_{10} \theta_{68} = p_0 + p_1 \log_{10} E + p_2 (\log_{10} E)^2 + p_3 (\log_{10} E)^3 \quad (10)$$

for $0.1 \leqslant E \leqslant 20$, where E is in GeV, $p_0 = -0.13$, $p_1 = -0.77$, $p_2 = 0.06$, and $p_3 = 0.04$. We approximate all simulated photon events to be within 45° of normal incidence, since the PSF containment angle θ_{68} is nearly constant from normal incidence out to 45° off axis.

We assume a point source to have a two-dimensional Gaussian (normal) distribution of gamma rays $f(x, y) = e^{-\left(\frac{x^2+y^2}{2\sigma^2}\right)}$, so the

---

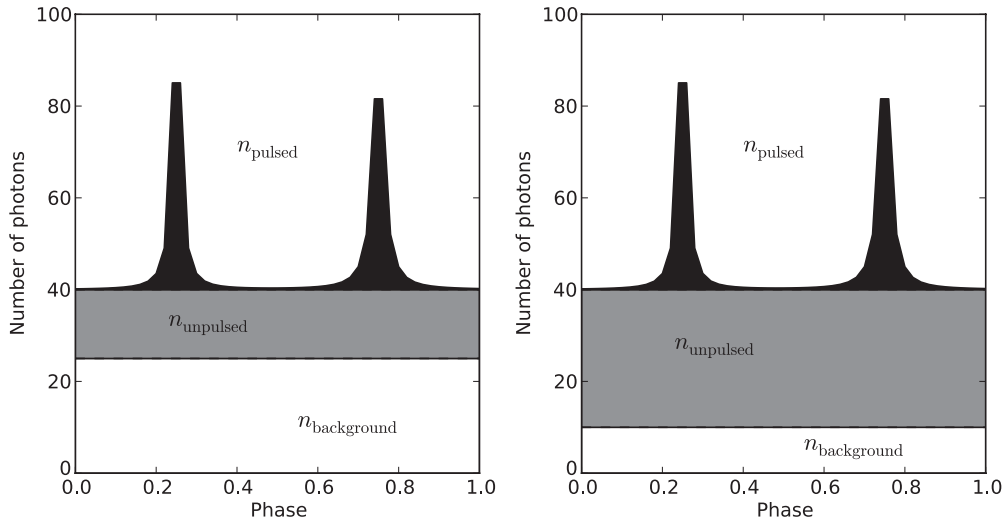[16] http://www-glast.slac.stanford.edu/software/IS/glast_lat_performance.htm

Figure 8. Sample pulse profiles for a simulated pulsar with an identical number of pulsed photons, n_{pulsed}, but different numbers of unpulsed photons, n_{unpulsed}, and background photons, $n_{\text{background}}$. Since n_{unpulsed} and $n_{\text{background}}$ are indistinguishable, both pulsars would be detected with equal probability. This motivates our definition of the detectability metric M as the ratio of pulsed photons to all photons.

ratio, R, of source photons falling within the ROI to all source photons is given as

$$R(r, \sigma) = \frac{\int_0^r r' \exp\left(-r'^2/2\sigma^2\right) dr' \int_0^{2\pi} d\theta}{\int_0^\infty r' \exp\left(-r'^2/2\sigma^2\right) dr' \int_0^{2\pi} d\theta}$$
$$= 1 - \exp\left(-r^2/2\sigma^2\right), \qquad (11)$$

where r is the angular separation from the source position, and the 68% containment angle in degrees is $\theta_{68} = 1.51\sigma$. The fraction of source photons falling within a $0°8$ radial cut is

$$R(r = 0°8, \theta_{68}) = 1 - \exp\left[-\frac{0.8^2}{2\left(\theta_{68}/1.51\right)^2}\right]$$
$$= 1 - \exp\left(-0.73/\theta_{68}^2\right), \qquad (12)$$

where $\log_{10}\theta_{68}$ is given in Equation (10). The number of detected photons above 300 MeV falling within $0°8$ is

$$n_{\text{signal}} =$$
$$k F_{100} \frac{\int_{0.3\,\text{GeV}}^{20\,\text{GeV}} R(r = 0°8, \theta_{68}) E^{-\Gamma} \exp\left[-(E/E_{\text{cutoff}})^\beta\right] dE}{\int_{0.1\,\text{GeV}}^{20\,\text{GeV}} E^{-\Gamma} \exp\left[-(E/E_{\text{cutoff}})^\beta\right] dE},$$
$$(13)$$

where $\log_{10} k = 10.47 \pm 0.12$ and k has units cm^2 s. k is a constant that represents the instrument effective area times the time spent observing a source, which depends on the incident angle and source spectrum. The spread in the fit is partially due to the assumption of normal incidence in Equation (10), non-uniform all-sky exposure during the first year of observations, and Poisson noise.

4.3. Sensitivity at High Frequencies

There is a marked drop-off in sensitivity to pulsars with high frequencies ($f > 16$ Hz), as seen in Figure 6. This is also shown in the detectability metric, where high-frequency pulsars are less detectable than low-frequency ones (see Figure 9). M depends only on the S/N and the PF, which is distributed independently from the frequency. In fact, at low frequencies
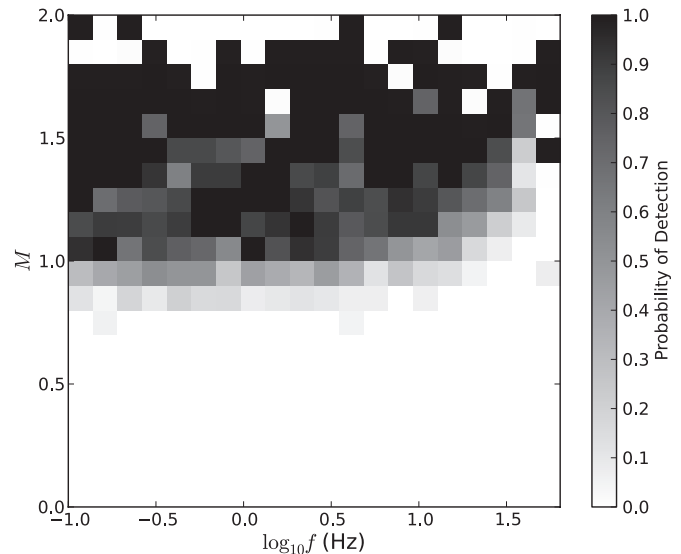

Figure 9. Density plot of detectability metric M vs. frequency f for all detected pulsars in the sample. For low frequencies, the detectability depends only on M, but for high frequencies, there is a drop-off in the number of detections.

the rate of detection depends only on the value of the metric M. But at high frequencies we observe a drop-off in the detection rate. This trend is more apparent at low S/N, where on average the source is weaker, the number of pulsed photons smaller, and the offset larger.

5. DISCUSSION

Our results can be interpreted in terms of the key factors affecting the sensitivity of our blind searches, with the purpose of providing a formula to estimate the sensitivity and an all-sky sensitivity map under standard assumptions. We model the sensitivity using the detectability metric M with a logistic sigmoid function assuming that the pulsar detections follow a binomial distribution with probability $P(M)$. Since multi-wavelength source locations, when available, should improve the search sensitivity, we repeated the same analysis using precise multiwavelength *counterpart* source locations. We explain

how an offset in position causes a Doppler shift modulation, which is more important for searches of high-frequency pulsars ($f > 16$ Hz). Using $P(M)$ and a set of assumptions for a given pulsar model, we construct an all-sky detectability map and provide the tools to determine the upper limits on pulsed fraction.

5.1. Modeling the Detectability

We estimate the detection probability associated with the metric M (Equation (9)) as a fit to the logistic sigmoid function, with the constraint $P(M \to -\infty) = 0$:

$$P(M) = \frac{A}{1 + \exp\left((\mu - M)/\sigma\right)}. \qquad (14)$$

Assuming that pulsar detections follow a binomial distribution with expected probability p, we maximize the likelihood function over the parameters A, μ, and σ. We estimate the 68% uncertainties in the parameters assuming that the likelihood is approximated by an asymmetric Gaussian around the maximum. We get the values $A = 0.857^{+0.023}_{-0.025}$, $\mu = 0.979^{+0.009}_{-0.010}$, and $\sigma = 0.057 \pm 0.006$. We also parameterized A, μ, and σ as linear functions of spin frequency in order to illustrate the effect of large spin frequencies on detectability. We obtain the fit values $A = A_1 f + A_2$ ($A_1 = -0.002 \pm 0.004$, $A_2 = 0.93 \pm 0.02$), $\mu = \mu_1 f + \mu_2$ ($\mu_1 = 0.01 \pm 0.002$, $\mu_2 = 0.94^{+0.02}_{-0.01}$), and $\sigma = \sigma_1 f + \sigma_2$ ($\sigma_1 = 0.001 \pm 0.001$, $\sigma_2 = 0.04^{+0.007}_{-0.006}$).

While a faint gamma-ray pulsar yields a poor LAT position, it might have a strong, well-localized, *counterpart* source in another waveband. We created such a counterpart location by sampling a random angular distance $0'' \leqslant r \leqslant 10''$ in a random orientation from the simulated pulsar location. This range is the typical positional uncertainty for X-ray instruments. These source locations are more accurate than the LAT locations and yield a higher detection probability. We performed the blind search on all pulsars using these simulated counterpart locations and detected 1359 pulsars (compare with 1121 using simulated LAT locations). We obtained fit parameters for the counterpart detectability metric by maximizing the likelihood function over the parameters A, μ, and σ to get the values $A = 0.949^{+0.015}_{-0.012}$, $\mu = 0.939 \pm 0.007$, and $\sigma = 0.048 \pm 0.004$ (see Figure 10). In addition, we parameterized A, μ, and σ as linear functions of spin frequency. We get $A = A_1 f + A_2$ ($A_1 = -0.005 \pm 0.002$, $A_2 = 1.0^{+0.0}_{-0.003}$), $\mu = \mu_1 f + \mu_2$ ($\mu_1 = 0.005 \pm 0.001$, $\mu_2 = 0.92 \pm 0.01$), and $\sigma = \sigma_1 f + \sigma_2$ ($\sigma_1 = 0.000 \pm 0.001$, $\sigma_2 = 0.042^{+0.006}_{-0.004}$). We fix $A_2 \leqslant 1.0$ in the fit and provide a lower limit.

To see the benefit of using counterpart source locations in blind searches, we searched for the known *Fermi* LAT pulsars (Abdo et al. 2010c; Saz Parkinson et al. 2010) using two locations: the simulated LAT location and the simulated counterpart location. Here, the simulated LAT location is obtained as in Section 3.1, and the counterpart location is randomized between $0''$ and $10''$ around the timed position. Using the optimized LAT location we detect all 26 blind search pulsars (Abdo et al. 2009a; Saz Parkinson et al. 2010; P. M. Saz Parkinson et al., in preparation), all 6 bright pulsars detected by EGRET (Nolan et al. 1996), and 5 radio-loud pulsars included in the 1FGL (Abdo et al. 2010c): PSRs J1028−5819, J1048−5832, J1509−5850, J2021+3651, and J2229+6114. Using the simulated counterpart locations, in addition to detecting the previous 35 pulsars, we also detect 2 additional radio-loud pulsars, J0659+1414 and J1420−6048.
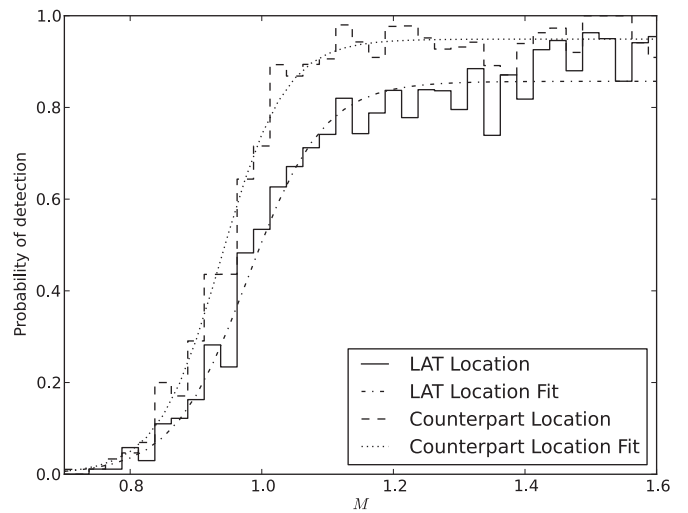

Figure 10. Detectability of pulsars in blind searches for optimized LAT locations and simulated counterpart locations. Counterpart locations to within $10''$ allow for higher detection probabilities for all values of the metric $M = \log_{10} n_{\text{pulsed}}/\sqrt{n}$.

5.2. Sensitivity to Positions

As shown in Section 4.1, the detectability of a pulsar depends greatly on the uncertainty in position. In Section 5.1, we showed that using multiwavelength counterpart locations reduces the effect of the Doppler shift frequency modulation and allows for dimmer pulsars to be detected. Details are described below.

The detection of high-frequency pulsars is more sensitive to positional errors (e.g., Ransom 2001; Chandler et al. 2001; Ray et al. 2011). The positional error of a pulsar smears the peak in the DFT by the amount

$$\delta f_{\text{pos}} = \frac{v}{c} f \epsilon |\sin\theta| = \frac{v}{c} f \epsilon \sqrt{1 - (\cos\phi \sin\omega t)^2}, \qquad (15)$$

where ϵ is given in radians, v is Earth's orbital velocity ($v/c \sim 10^{-4}$), and θ is the angle between v and the source direction. The angle θ is a combination of the azimuthal angle ωt and the polar angle ϕ, where $\omega = 2 \times 10^{-7}$ rad s^{-1}. In this convention, an object directly overhead the ecliptic plane is located at $\phi = \frac{\pi}{2}$ and an object within the plane of the solar system is located at $\phi = 0$.

The corresponding shift in frequency derivative due to positional error is calculated by differentiating Equation (15):

$$\delta \dot{f}_{\text{pos}} = 10^{-4} \epsilon (f \dot{\theta} \cos\theta + \dot{f} \sin\theta). \qquad (16)$$

The second term is negligible when compared with the first, as $\dot{f} \sim 10^{-12}$ and $\dot{\theta} \sim 10^{-7}$:

$$\delta \dot{f}_{\text{pos}} = -10^{-4} \epsilon f \frac{\omega \cos^2\phi |\cos\omega t \sin\omega t|}{\sqrt{1 - (\cos\phi \sin\omega t)^2}}. \qquad (17)$$

If the frequency is shifted by more than a few DFT bins, the power is significantly reduced. The maximum frequency shift δf due to positional error is when $\sin\theta = 1$:

$$|\delta f_{\text{max}}| = \frac{v}{c} \epsilon f. \qquad (18)$$

The number of frequency bins shifted is equal to δf_{max} divided by the frequency resolution $\Delta f = 1/2T_{\text{maxdiff}}$. If we require the
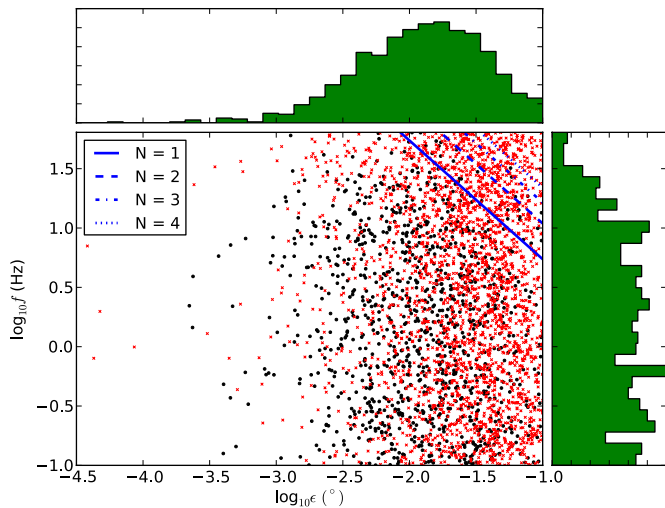
Figure 11. Spin frequency vs. position offset for all detected pulsars (black dots), and maximum positional error due to the Doppler shift for a given number of shifted bins N (dashed lines) found in Equation (21). In this simulation of 10,000 pulsars, most of the detected pulsars had a shift of less than one frequency bin.

(A color version of this figure is available in the online journal.)

frequency shift by no more than N frequency bins

$$\frac{\delta f_{max}}{\Delta f} \leqslant N \qquad (19)$$

$$\epsilon \leqslant \frac{N}{2 T_{maxdiff}(v/c)f}. \qquad (20)$$

Setting $T_{maxdiff} = 2^{19}$ s, $v/c = 10^{-4}$ and converting from radians to degrees

$$\epsilon \leqslant \frac{0.54 \times N}{f}, \qquad (21)$$

where ϵ is given in degrees and f is given in Hz. The plot of all detected pulsar frequencies versus positional offset is shown in Figure 11, with a selection of different N values.

While pulsar searches are sensitive to position errors, one important result from Equation (21) is that as the frequency of the pulsar increases we require a position with greater certainty. Therefore, we can increase our sensitivity to high-frequency pulsar detections by homing in on the position. This idea is illustrated in the plot of position offset and frequency for all detected pulsars (Figure 11). As both f and the position offset become large, there is a drop-off in the number of detections. This is due to both the inability to combine enough higher harmonics with a fixed maximum search frequency $f_{max} = 64$ Hz and the sensitive dependence on position.

5.3. Sensitivity Recipe

The steps in obtaining the pulsar detection probability P are summarized as follows.

1. Assume a spectral model and pulsed fraction, e.g., $\Gamma = 1.5$, $E_{cutoff} = 2$ GeV, $\beta = 1$, $F_{100} = 3 \times 10^{-8}$ photon cm^{-2} s^{-1}, and PF = 0.5.
2. Measure the total number of photons n within the ROI and estimate the number of signal photons using Equation (13).
3. Calculate the value of the metric M using Equation (9).
4. Apply Equation (14) with the corresponding A, μ, and σ values for the source positions to determine P.

This recipe is only for a blind search using the time differencing method for one year of LAT photon data processed with the P6_V3 *diffuse* IRF. We can use this recipe to measure detection 1σ upper limits on the pulsed fraction by fixing the detection probability at $P(M) = 0.68$ and solving for M with a tail probability of 0.32. For a 1σ detection, $M_{68} = 1.056$ for LAT source locations and $M_{68} = 0.985$ for counterpart locations.

5.4. Detectability Map

As an application of Section 5.3, we generated an all-sky detectability flux map assuming a spectral model and pulse profile. An all-sky blind search sensitivity map is useful in determining the probability of detection for a given source location. We binned the sky above 300 MeV in $0°.1 \times 0°.1$ bins and calculated all counts n within the $0°.8$ ROI for each pixel. The minimum number of signal photons required to detect a
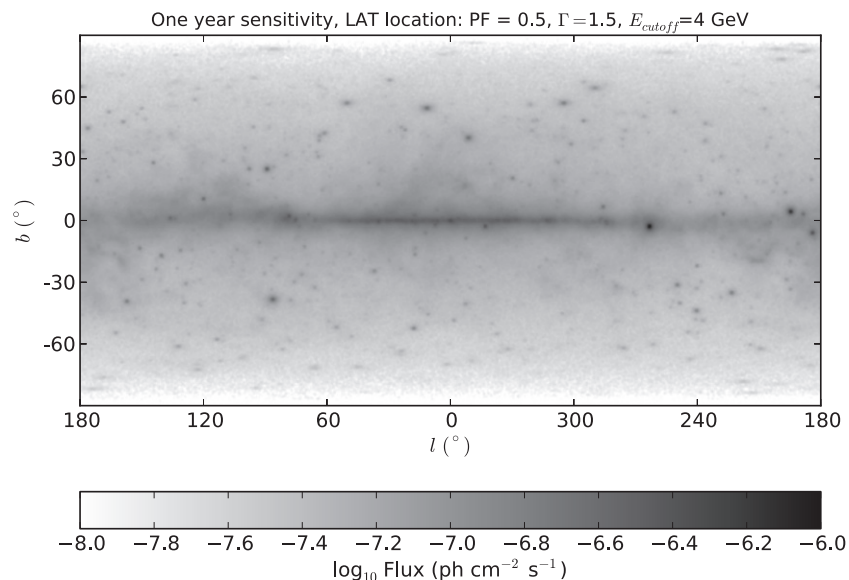

Figure 12. Minimum flux required for a pulsar detection for a given position on the sky, assuming $P(M) \geqslant 0.5$, PF = 0.5, $\Gamma = 1.5$, $E_{cutoff} = 4$ GeV, and $\beta = 1$. Note the higher minimum flux required for sources in the inner Galactic plane.

10

pulsar with $P(M) > 0.5$ is given by solving Equation (9) for n_{signal}:

$$n_{\text{signal}} = \frac{10^M \times \sqrt{n}}{\text{PF}}, \qquad (22)$$

where n_{signal} is converted to minimum flux F_{min} using Equation (13):

$$F_{\text{min}} = \frac{1}{k} \frac{10^M \times \sqrt{n}}{\text{PF}}$$
$$\times \frac{\int_{0.1\,\text{GeV}}^{20\,\text{GeV}} E^{-\Gamma} \exp\left[-(E/E_{\text{cutoff}})^\beta\right] dE}{\int_{0.3\,\text{GeV}}^{20\,\text{GeV}} R(r = 0.^{\!\circ}8, \theta_{68}) E^{-\Gamma} \exp\left[-(E/E_{\text{cutoff}})^\beta\right] dE},$$
$$(23)$$

where $P(M) = 0.5$ corresponds to $M \sim 1$ for LAT locations (see Figure 10.) This map is shown in Figure 12, assuming $P(M) \geqslant 0.5$, PF $= 0.5$, $\Gamma = 1.5$, $E_{\text{cutoff}} = 4$ GeV, and $\beta = 1$.

For counterpart sources, $P(M) = 0.5$ corresponds to $M \sim 0.944$. At the threshold probability of $P(M) = 0.5$ the ratio of minimum signal for a counterpart source location to minimum signal for a LAT source location is $10^{0.944}/10 \approx 0.88$, which indicates the counterpart locations allow for up to a $\sim 12\%$ dimmer flux detection threshold. This is especially useful for sources located within the Galactic plane as diffuse Galactic emission can obscure faint pulsars.

6. CONCLUSION

We have established the sensitivity of the time-differencing technique of blind searches for gamma-ray pulsars using a Monte Carlo simulation of pulsar sources. We measured and modeled the sensitivity of the blind search of gamma-ray data alone using a large-scale simulation of *Fermi* LAT pulsars and source locations. We simulate each pulsar's source position using the detection and localization tools used in the creation of the LAT 1FGL catalog. The factors that fully determine the sensitivity are the detectability metric M in Equation (9) and the spin frequency f. At high frequencies, we observe a drop-off in the detection rate, which is more apparent for fainter sources with larger positional offsets.

Weak sources with low TS values tend to have less accurate source locations than bright sources with high TS values (Figure 5). Counterpart source locations, when available, improve our knowledge of the putative pulsar position, thus reducing the Doppler shift frequency modulation, making a pulsar easier to detect. This trend is confirmed with searches of isolated, non-binary MSPs up to a maximum search frequency $f_{\text{max}} = 1024$ Hz (not included in this study). Even incorporating four harmonics, we can still observe the drop-off in sensitivity for a small positional error.

A large number of unassociated *Fermi* LAT sources exhibit pulsar-like characteristics, such as non-variable flux and an exponentially cutoff power-law spectrum, leading us to suspect that they may be pulsars. Using our sensitivity maps allows us to place upper limits on their possible pulsar properties, including pulsed fraction (see Section 5.3). Unidentified sources with a low M could indicate that if they are pulsars, the pulsed fraction or S/N is too small to be detected in a blind search. Conversely, there could be unassociated sources in the 1FGL catalog with a high M and might therefore be undetected pulsars. This study provides motivation for focusing on promising sources in order to uncover their pulsations, especially sources long suspected to be pulsars.

The extension of the one-year sensitivity to multi-year sensitivity is non-trivial, as other factors besides simply finer stepping in $\dot{f}$ become important beyond one year. Current blind search efforts using multi-year LAT data include searching up to and beyond MSP spin frequencies, searching with higher order frequency derivative corrections ($\ddot{f}$), using larger coherence windows for the differencing method (up to $T_{\text{maxdiff}} = 2^{21}$ s $\sim$24 days), scanning in position for a selection of choice candidates, or using a weighted photon selection method (Kerr 2011). These modifications to the blind search code should be incorporated into a multi-year sensitivity study.

Multiwavelength counterpart positions (especially in X-rays) of interesting sources become increasingly necessary to refine *Fermi* LAT positions. Such observations are an important key ingredient that will help the LAT unveil the remaining blind search pulsars hidden in the gamma-ray sky.

REFERENCES

Abdo, A. A., Ackermann, M., Ajello, M., et al. 2009a, Science, 325, 840
Abdo, A. A., Ackermann, M., Ajello, M., et al. 2009b, ApJS, 183, 46
Abdo, A. A., Ackermann, M., Ajello, M., et al. 2010a, ApJS, 188, 405
Abdo, A. A., Ackermann, M., Ajello, M., et al. 2010b, ApJ, 713, 154
Abdo, A. A., Ackermann, M., Ajello, M., et al. 2010c, ApJS, 187, 460
Abdo, A. A., Ackermann, M., Ajello, M., et al. 2010d, ApJ, 720, 272
Abdo, A. A., Ackermann, M., Ajello, M., et al. 2011, Science, 331, 739
Abdo, A. A., Ackermann, M., Atwood, W. B., et al. 2009c, ApJ, 696, 1084
Ackermann, M., Ajello, M., Baldini, L., et al. 2011, ApJ, 726, 35
Atwood, W. B., Abdo, A. A., Ackermann, M., et al. 2009, ApJ, 697, 1071
Atwood, W. B., Ziegler, M., Johnson, R. P., & Baughman, B. M. 2006, ApJ, 652, L49
Benjamini, Y., & Hochberg, Y. 1995, J. R. Statist. Soc. Ser. B, 57, 289
Bertin, E., & Arnouts, S. 1996, A&AS, 117, 393
Chandler, A. M., Koh, D. T., Lamb, R. C., et al. 2001, ApJ, 556, 59
Ciprini, S., Tosti, G., Marcucci, F., et al. 2007, in AIP Conf. Ser. 921, The First GLAST Symposium, ed. S. Ritz, P. Michelson, & C. A. Meegan (Melville, NY: AIP), 546
Damiani, F., Maggio, A., Micela, G., & Sciortino, S. 1997, ApJ, 483, 350
Edwards, R. T., Hobbs, G. B., & Manchester, R. N. 2006, MNRAS, 372, 1549
Espinoza, C. M., Lyne, A. G., Stappers, B. W., & Kramer, M. 2011, MNRAS, 414, 1679
Gonthier, P. L., Van Guilder, R., & Harding, A. K. 2004, ApJ, 604, 775
Górski, K. M., Hivon, E., Banday, A. J., et al. 2005, ApJ, 622, 759
Harding, A. K., Grenier, I. A., & Gonthier, P. L. 2007, Ap&SS, 309, 221

Holwerda, B. W. 2005, arXiv:astro-ph/0512139

Kerr, M. 2011, ApJ, 732, 38

Lorimer, D. R., & Kramer, M., (ed.) 2004, Handbook of Pulsar Astronomy (Cambridge: Cambridge Univ. Press)

Manchester, R. N., Hobbs, G. B., Teoh, A., & Hobbs, M. 2005, AJ, 129, 1993

Muslimov, A. G., & Harding, A. K. 2003, ApJ, 588, 430

Nolan, P. L., Fierro, J. M., Lin, Y. C., et al. 1996, A&AS, 120, C61

Paczynski, B. 1990, ApJ, 348, 485

Pletsch, H. J., Guillemot, L., Allen, B., et al. 2011, ApJ, in press (arXiv:1111.0523)

Ransom, S. M. 2001, Ph.D. thesis, Harvard Univ. (ProQuest Dissertations and Theses, publication number AAT3028434)

Ray, P. S., Kerr, M., Parent, D., et al. 2011, ApJS, 194, 17

Razzano, M., & Harding, A. K. 2007, in AIP Conf. Ser. 921, The First GLAST Symposium, ed. S. Ritz, P. Michelson, & C. A. Meegan (Melville, NY: AIP), 413

Razzano, M., Harding, A. K., Baldini, L., et al. 2009, Astropart. Phys., 32, 1

Saz Parkinson, P. M., Dormody, M., Ziegler, M., et al. 2010, ApJ, 725, 571

Starck, J., & Pierre, M. 1998, A&AS, 128, 397